IEEE Photonics Journal
An IEEE Photonics Society Publication

Open Access

A Mid-Infrared Dual-Band Filter With Ultra-High Resolving Power

Volume 12, Number 4, August 2020

Xin He
Jinliang Jie
Junbo Yang
Yunxin Han
Sen Zhang

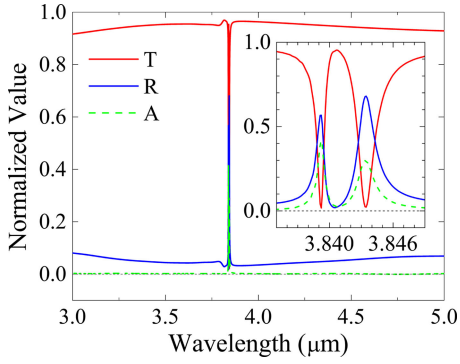

DOI: 10.1109/JPHOT.2020.3006890

A Mid-Infrared Dual-Band Filter With Ultra-High Resolving Power

Xin He,[1] **Jinliang Jie**,[2] **Junbo Yang**,[1] **Yunxin Han**,[1] **and Sen Zhang**[1]

[1]Department of Physics, National University of Defense Technology, Changsha 410073, China
[2]College of Aerospace Science and Engineering, National University of Defense Technology, Changsha 410073, China

DOI:10.1109/JPHOT.2020.3006890

Manuscript received May 21, 2020; accepted June 29, 2020. Date of publication July 3, 2020; date of current version July 23, 2020. This work was supported in part by the National Natural Science Foundation of China (NSFC) under Grants 60907003, 61671455, and 61805278, in part by the Program for New Century Excellent Talents in University (NCET) (NCET-12-0142), and in part by the China Postdoctoral Science Foundation under Grant 2018M633704. Corresponding author: Junbo Yang (e-mail: yangjunbo@nudt.edu.cn).

Abstract: A mid-infrared (mid-IR) dual-band filter with ultra-high resolving power is designed and numerically investigated. It is composed of an Al_2O_3 layer between a gold grating and a CaF_2 substrate. Each unit cell of the grating consists of two gold strips with different heights. The filter provides two high-extinction ultra-narrow stop bands. One is at a wavelength of $\sim$3.8392 μm with a full-width at half-maximum (FWHM) of $\sim$0.8 nm, and the other is at a wavelength of $\sim$3.8435 μm with a FWHM of $\sim$1.8 nm. The resolving power of the filter is $>$2100. The two stop bands result from the $(+1)$ and (-1) waveguide modes, respectively. An interaction between the two resonance modes exists and affects the stop bands. We can control the interaction by adjusting the grating parameters, thus designing the FWHMs and lineshapes of the two stop bands flexibly.

Index Terms: Subwavelength structures, filters, spectroscopy.

1. Introduction

Recently, there has been an increasing interest in using subwavelength grating structures to realize optical filters. Compared with traditional filters made of multi-layered thin films [1], subwavelength grating structure filters have the obvious advantages of low material cost, thin thickness, and flexible control of spatial variation [2]. Researchers have investigated the use of dielectric gratings in such type of filters. Spectral filtering is achieved based on the guided-mode resonance (GMR) effect [3]–[6]. Alternatively, metallic structures can also be used, and spectral filtering is achieved based on the surface-plasmon resonance (SPR) effect [2], [7]–[9].

It should be noted that, in many hyper-spectral applications, optical filters with high resolving power are highly desirable [8], [10]. These filters can provide narrow operating bands, thus enabling precise selection or rejection of light at certain wavelengths. To achieve such filters, the quality-factor (Q-factor) on resonance must be improved. For this reason, dielectric grating filters have attracted extensive attention due to their intrinsic low-loss [11]–[14]. However, bandstop or bandpass filters based on metallic structures could also have ultra-narrow operating bands [15], [16]. Dielectric grating filters in the literature typically suffer from unwanted peaks over broad

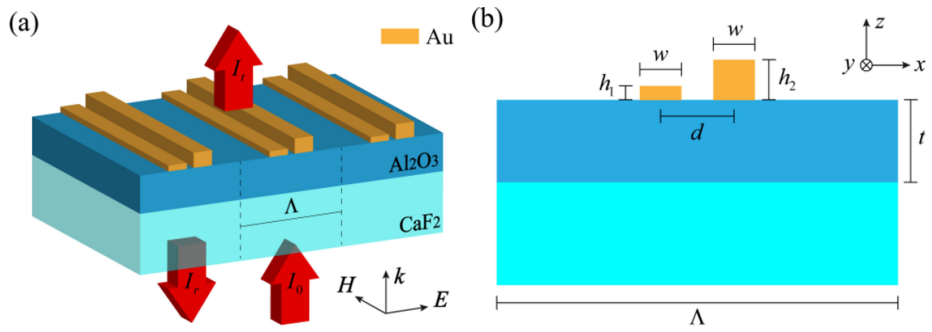

Fig. 1. (a) Schematic view of the designed mid-IR dual-band filter. I_0, I_t, and I_r stand for intensities of the incidence, transmission, and reflection, respectively. Λ is the period of the structure. (b) Cross-sectional view of a single unit cell of the filter.

spectral regions [11]. Metallic structure filters suffer from the same issue [8]. But notably, there has been research showing that this issue could be solved by proper design of the metallic structure [2].

However, most of the above-mentioned subwavelength structure filters only have a single and narrow operating band. For high-resolution spectroscopic multiplexing sensing and detection, we usually need filters with dual or multiple operating bands, ultra-narrow bandwidths, and no unwanted peaks over broad spectral regions. Filters with these characteristics can give us the ability to precisely control multi-wavelength signals, such as laser signals, atomic lines, molecular lines, etc. From this point of view, it is hard to use the above-mentioned filters. The use of metal-insulator-metal (MIM) structures could generate dual or multiple bands [17]–[19], but the spectral resolving power is usually below 100.

In this work, we propose an ultra-high resolving power dual-band filter operating in the mid-IR spectral region. It is achieved by the use of a new gold grating consisting of two gold strips with different heights in each cell. The two ultra-narrow stop bands are attributed to the $(+1)$ and (-1) waveguide modes excited by the incidence, respectively. The resolving power of the filter can be higher than 2100. Moreover, the two resonance modes can interact with each other. The interaction affects the FWHMs and lineshapes of the two stop bands. By adjusting the geometric parameters of the gold grating, the interaction can be controlled. Therefore, the FWHMs and lineshapes of the filter can be designed flexibly.

2. Results and Analysis

Fig. 1(a) shows the designed mid-IR dual-band filter. It consists of an Al_2O_3 layer between a gold grating and a CaF_2 substrate. The structure (grating) has a period of Λ. The incidence is a transverse magnetic (TM) plane wave, whose polarization is perpendicular to the gold strips. In each unit cell of the grating, there are two gold strips, and the center-to-center distance between them is d, as shown in Fig. 1(b). The two gold strips have the same width (i.e., w) but different heights (i.e., h_1 and h_2). The thickness of the Al_2O_3 layer is t. The performance of the filter was simulated by means of a finite-difference time-domain (FDTD) method. In the simulations, optical parameters of gold and Al_2O_3 were taken from Ref. [20], whereas optical parameters of CaF_2 were taken from Ref. [21].

Fig. 2 shows the calculated reflection, transmission, and absorption spectra at normal incidence. The structure parameters are as follows: $\Lambda = 2.7$ μm, $t = 1.0$ μm, $w = 220$ nm, $d = 270$ nm, $h_1 = 50$ nm, and $h_2 = 230$ nm. There are only two notable transmission dips across the 3-5 μm wavelength range. The transmission background is high ($>$90%). One of the dips is approximately at $\lambda_1 = 3.8392$ μm, with a FWHM of $\sim$0.8 nm and a minimum transmission of $<$1.8%. The quality-factor (Q-factor) calculated by λ_1/FWHM is $>$4700, and the intensity-extinction on resonance calculated by $10\log_{10}(I_0/I_t)$ is $>$17 dB. The other dip is approximately at $\lambda_2 = 3.8435$ μm,

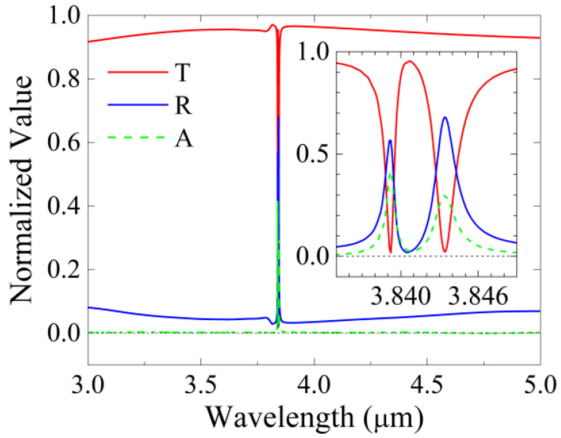

Fig. 2. Calculated transmission (T), reflection (R), and absorption (A) spectra at normal incidence. Inset shows magnified view of the two ultra-narrow operating bands.

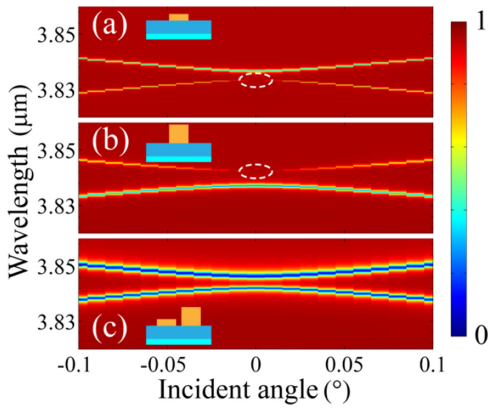

Fig. 3. Angle-dependent transmission without the thicker (a) or the thinner (b) gold strip. The dotted ellipses mark the symmetry-protected BICs. (c) Angle-dependent transmission of our structure.

with a FWHM of $\sim$1.8 nm and a minimum transmission of $<$2.3%. Its Q-factor is $>$2100, and its intensity-extinction on resonance is $>$16 dB. The spectral separation of the two dips is $\sim$4.3 nm, which is nearly three orders of magnitude smaller than the operating wavelengths.

Moreover, the reflection spectrum in Fig. 2 shows two ultra-narrow peaks with low reflection background, which will be useful in mid-IR filtering applications too. However, because resonance absorption exists, the maximum reflection of the two peaks is $<$70%.

To understand the mechanism of the two ultra-narrow operating bands, Figs. 3(a) and 3(b) show the angle-dependent transmission maps after removing the thicker and thinner gold strips in each unit cell, respectively. For comparison, the angle-dependent transmission map of our structure is plotted in Fig. 3(c).

The transmission dips in Fig. 3 can be attributed to the GMR effect. That is, when an order diffracted by the gold grating couples with a waveguide mode in the Al_2O_3 layer, the resonances occur. The resonance wavelengths can be determined by the wavevector matching condition [8], [15], [16]

$$\left|\beta_{\parallel}\right| = \left|k_{\parallel} + \frac{2\pi i}{\Lambda}\right| \tag{1}$$

where $\beta_{\parallel}$ and $k_{\parallel}$ are the in-plane wavevectors of the resonance mode and the incidence, i is the index of diffraction order. In our case, the resonance modes excited by the $(+1)$ and (-1) orders

should be under consideration. So there are

$$\frac{2\pi n_{\text{eff}}^{(+1)}}{\lambda^{(+1)}} = \left| k \sin\alpha + \frac{2\pi}{\Lambda} \right| \tag{2}$$

$$\frac{2\pi n_{\text{eff}}^{(-1)}}{\lambda^{(-1)}} = \left| k \sin\alpha - \frac{2\pi}{\Lambda} \right| \tag{3}$$

where n_{eff} and λ are the effective index and center wavelength of the resonance mode, k and α are the wavevector and angle of the incidence.

In the case of Figs. 3(a) or 3(b), a symmetry-protected bound state in the continuum (BIC) is supported because of the symmetric configuration in each unit cell [22]–[24]. Thus, at normal incidence ($\alpha = 0°$), only a single transmission dip due to the GMR can be seen. The BIC happens in the shorter-wavelength band edge, as shown in Fig. 3(a). On the contrary, the BIC happens in the longer-wavelength band edge, as shown in Fig. 3(b). Both of the two BICs are unstable and can be transformed into quasi-BICs, if the structural symmetry in each unit cell is broken [25]–[27]. In our structure, structural asymmetry in each unit cell is introduced by using two gold strips with different heights. This leads to quasi-BICs in both the shorter- and longer-wavelength band edge. In other words, GMRs in our structure can happen in both the shorter- and longer-wavelength band edge. Therefore, even at normal incidence, there are two spectral dips in the transmission, as shown in Fig. 3(c).

In Fig. 3(c), both of the transmission dips have ultra-high Q-factors. The reason is that the losses of the resonance modes are ultra-low [28]. Firstly, the Al_2O_3 layer in our structure has a relatively low index and large thickness. The resonant energy is mainly confined in the Al_2O_3 layer, as shown in the insets of Fig. 3(c). Secondly, the optical loss of Al_2O_3 is very small in the 3-5 μm wavelength range. Compared with those in Fig. 3(c), although the Q-factors in Figs. 3(a) and 3(b) are higher, the intensity-extinctions are significantly lower. From the point of view of bandstop filtering, the structures shown in Figs. 3(a) and 3(b) are disadvantageous.

Based on Fig. 3(c), we can identify the resonance modes associated with the two transmission dips. We first consider the $(+1)$ mode. According to Eq. (2), as α increases from 0° to 90°, $n_{\text{eff}}^{(+1)}/\lambda^{(+1)}$ should increase. Since the mode is mainly confined in the Al_2O_3 layer, the effective index will increase/decrease with decreased/increased wavelength. To satisfy Eq. (2), $\lambda^{(+1)}$ should decrease with increased α. In other words, the transmission dip associated with the $(+1)$ mode should exhibit a blueshift with increased incident angle. Similarly, according to Eq. (3), we know that the transmission dip associated with the (-1) mode should exhibit a redshift with increased incident angle. Hence, the $(+1)$ mode is associated with the dip at shorter wavelength, and the (-1) mode is associated with the dip at longer wavelength. At normal incidence, there are $\lambda^{(+1)} = 3.8392$ μm and $\lambda^{(-1)} = 3.8435$ μm.

Additional understanding of the resonance properties is shown in Fig. 4. In Fig. 4(a), the electric field confined in the Al_2O_3 layer illustrates the $(+1)$ mode. There is also a strong concentration of the electric field at the gold ridges. This implies that displacement currents exist in the gold strips. In Fig. 4(b), we show the displacement currents. Owing to the Ohmic loss, a portion of the resonant energy is dissipated in the gold strips, as shown in Fig. 4(c). As a result, resonance absorption occurs. In Figs. 4(d)–4(f), similar phenomena are seen for the (-1) mode. A comparison between Figs. 4(b) and 4(e) reveals that the displacement currents have different distributions. Accordingly, the energy dissipations at the two resonance wavelengths are different, as shown in Figs. 4(c) and 4(f). The total energy loss at $\lambda^{(+1)} = 3.8392$ μm is larger than that at $\lambda^{(-1)} = 3.8435$ μm. Thus, the reflection at $\lambda^{(+1)} = 3.8392$ μm is smaller than that at $\lambda^{(-1)} = 3.8435$ μm.

3. Discussion

The geometric parameters of the gold strips in each unit cell can affect the spectral response of the structure. We adjusted d, w, h_1, or h_2 independently with the other parameters kept unchanged,

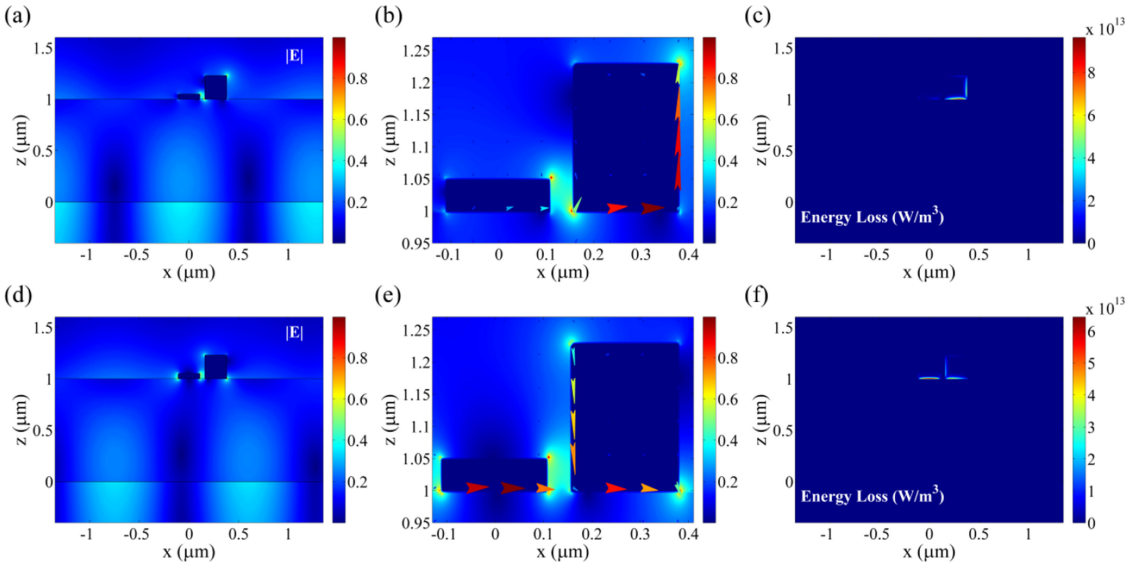

Fig. 4. Electric field (a), displacement current (b), and energy dissipation (c) distributions at $\lambda^{(+1)} = 3.8392\ \mu$m. (d), (e), and (f) are the same as (a), (b), and (c), but are at $\lambda^{(-1)} = 3.8435\ \mu$m.

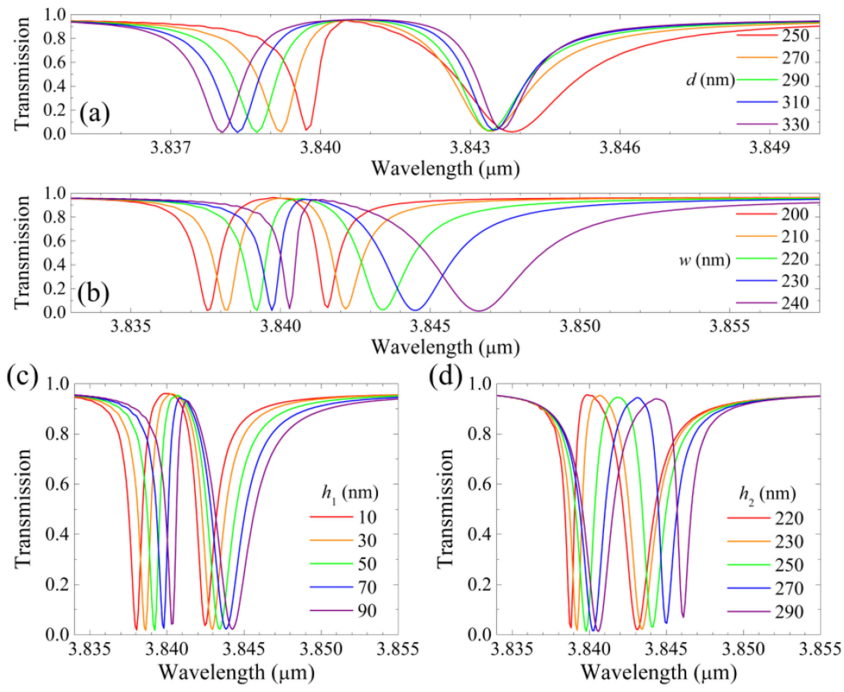

Fig. 5. Transmission with different values of d (a), w (b), h_1 (c), and h_2 (d).

and calculated the transmission spectra. The results are shown in Fig. 5. According to the analysis above, we should note that $\lambda^{(+1)}$ and $\lambda^{(-1)}$ in the following stand for the stop bands at shorter and longer wavelengths, respectively.

In Fig. 5(a), as d decreases, $\lambda^{(+1)}$ exhibits a redshift. However, $\lambda^{(-1)}$ almost does not show a redshift unless d is small enough. According to Eqs. (2) and (3), the redshifts are attributed to the

increases in $n_{\text{eff}}^{(\pm 1)}$. A smaller d leads to a stronger electric field in the gold slit, thus increasing $n_{\text{eff}}^{(\pm 1)}$. However, the electric field distributions in the gold slit are different (Figs. 4(b) and 4(e)). When d increases, the changes in $n_{\text{eff}}^{(+1)}$ and $n_{\text{eff}}^{(-1)}$ are different. As a result, there is a difference between the shifts of the two dips.

In Figs. 5(b)–5(d), the two dips exhibit redshifts when w, h_1, or h_2 increases. The reason is that the volume of gold (i.e., $wh_1 + wh_2$) in each unit cell increases. This leads to the increases in $n_{\text{eff}}^{(\pm 1)}$, thus enlarging $\lambda^{(\pm 1)}$ in Eqs. (2) and (3). In Figs. 5(b) and 5(d), it is observed that $\lambda^{(-1)}$ is more sensitive to w or h_2. There are two reasons. At first, the electric field at $\lambda^{(-1)}$ is close to the thicker gold strip, as shown in Fig. 4(d). Then, as w or h_2 increases, the increase in wh_2 is always larger. Thus, the increase in $n_{\text{eff}}^{(-1)}$ is larger when w or h_2 increases.

In Fig. 5, significant changes in the FWHMs and lineshapes of the two dips are seen. These changes can be attributed to the interaction between the $(+1)$ and (-1) modes. The interaction is caused by the following two aspects. Firstly, the resonance wavelengths of the two modes are very close to each other. Secondly, the electromagnetic fields on resonance are bonded to both of the gold strips. In particular, the electric fields in the slit are strong and show different distributions. Therefore, the interaction could be associated with the gold slit.

We would estimate that the volume of the slit associated with the $(+1)$ mode is

$$V_{\text{slit}}^{(+1)} = h_1(d - w) \tag{4}$$

and the volume of the slit associated with the (-1) mode is

$$V_{\text{slit}}^{(-1)} = \frac{1}{2}(h_1 + h_2)(d - w) \tag{5}$$

Thus, the difference between $V_{\text{slit}}^{(+1)}$ and $V_{\text{slit}}^{(-1)}$ is

$$\Delta V_{\text{slit}} = \frac{1}{2}(h_2 - h_1)(d - w) \tag{6}$$

In Fig. 5(a), when d is relatively small, ΔV_{slit} in Eq. (6) is relatively small. The interaction between the $(+1)$ and (-1) modes is strong. The lineshapes of the dips are asymmetric. In this situation, it should be noted that the dip at longer wavelength is broader than the dip at shorter wavelength. As $d$increases, ΔV_{slit} increases and is moderate. The interaction weakens. The lineshapes are relatively symmetric, and the two dips could have the same FWHM. In Figs. 5(b)–5(d), similar phenomena are seen when ΔV_{slit} is relatively small.

In Fig. 5(b), when w is small, ΔV_{slit} is large. In this situation, the interaction is also strong, and the lineshapes of the dips are also asymmetric. However, the dip at longer wavelength can be narrower than the dip at shorter wavelength, which is different from the case of small ΔV_{slit}. In Fig. 5(d), this phenomenon is more obvious when ΔV_{slit} is large. The results indicate that we can tune the FWHMs and lineshapes of the two transmission dips flexibly.

Fig. 6 shows the spectral responses of the structure with different Al_2O_3 thicknesses. The other structure parameters are kept unchanged. As t increases, the two dips exhibit significant redshifts. It is because a thicker Al_2O_3 layer leads to larger effective indices in Eqs. (2) and (3). The FWHM and lineshape of the dip at longer wavelength changes with increased t, which is similar to the phenomenon when ΔV_{slit} decreases. This is because the resonance wavelength increases. However, the FWHM and lineshape of the dip at shorter wavelength do not change significantly with increased t. This implies that the mode interaction changes slightly with increased t. A very small t is disadvantageous, since it lowers the intensity extinctions of the dips greatly.

The filter is obviously polarization-sensitive due to the one-dimensional gold grating. Fig. 7 shows the transmission spectrum of the filter when the incidence is a transverse-electric (TE) plane wave. As can be seen, there are two new transmission dips in this case, which are caused by the phase resonance effect [29]. Specifically, for the spectral dip at the shorter wavelength, the phase difference is approximately π (see inset I), and the electric field is opposite in each unit cell (see insets II and III). These result in significantly destructive interference in the transmission at this

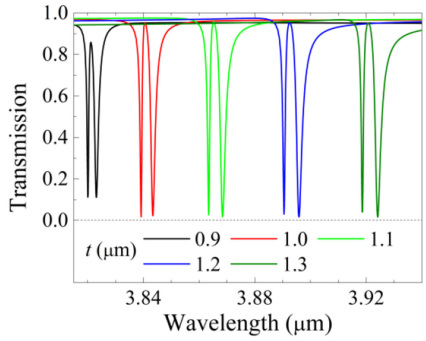

Fig. 6. Transmission with different thicknesses of the Al_2O_3 layer.

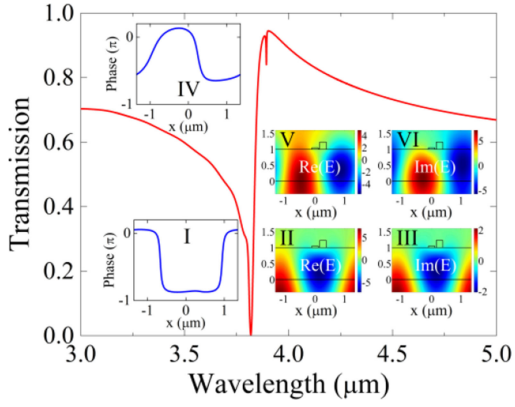

Fig. 7. The transmission spectrum in the case of a TE-polarized normal incidence. Insets: phase distribution at $z = 1.3$ μm (I) and electric field distributions (II and III) for the lower spectral dip; (IV)-(VI) are the same as (I)-(III) but are for the upper spectral dip.

wavelength. However, for the spectral dip at the longer wavelength, the phase difference deviates from π largely (see inset IV), although the electric field is opposite in each unit cell (see insets V and VI). Thus, the interference in the transmission at this wavelength is not strong enough to produce a high-extinction dip.

In addition, Figs. 4(b) and 4(e) indicate that strong electric fields are concentrated at the corners of the gold strips. However, considering practical situations, the corners of the fabricated gold strips cannot be as perfect as in Figs. 4(b) and 4(e). To investigate this, we carried out simulations where the gold strips in each unit cell were assumed to have trapezoidal cross-sections, rounded corners, or rough surfaces. In the case of trapezoidal cross-sections, the side slope was set to $\sim$10°. In the case of rounded corners, a radius of 20 nm was assumed. In the case of rough surfaces, random fluctuations within 15 nm were used. Fig. 8 shows the simulated transmission spectra. In these cases, we see that the filter still performs well. The transmission dips only shift slightly ($<$2 nm). The intensity extinctions on-resonance exhibit tiny changes. The Q-factors are equivalent to those in Fig. 2.

If we fabricate the filter, the Al_2O_3 layer could be obtained by deposition. However, the optical constants of a deposited Al_2O_3 layer may be different from those in Ref. [20]. In this situation, the geometric parameters of the structure should be slightly adjusted to achieve two transmission dips with good properties. Fig. 9(a) shows the transmission spectrum of the filter with a deposited Al_2O_3 layer, where the geometric parameters are: $\Lambda = 2.7$ μm, $t = 1.2$ μm, $w = 240$ nm, $d = 300$ nm, $h_1 = 50$ nm, and $h_2 = 250$ nm. It can be seen that the two transmission dips are ultra-narrow. Compared with those in Fig. 2, the Q-factors are slightly lower in this case. This is mainly because the width of the gold strips is slightly larger in this case.

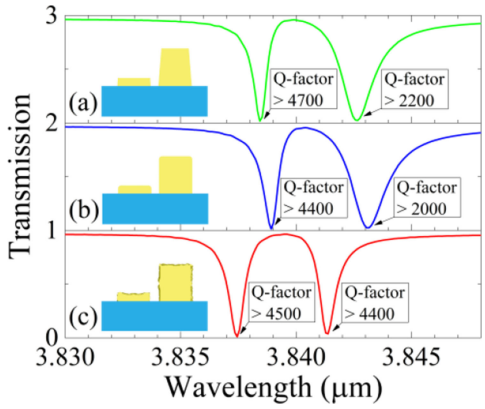

Fig. 8. Simulated transmission spectra assuming that the fabricated gold strips have: Trapezoidal cross-sections (a), rounded corners (b), and rough surfaces (c). The other structure parameters are the same as those used in Fig. 2.

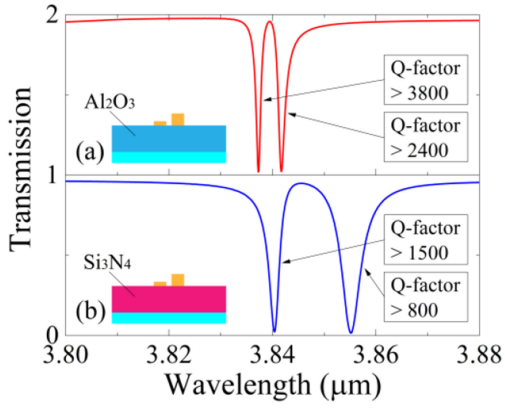

Fig. 9. Simulated transmission spectra assuming that the waveguide layer between the gold grating and the substrate is a deposited Al_2O_3 film (a) and Si_3N_4 film (b). Note that the optical constants from Refs. [30] and [31] are used for Al_2O_3 and Si_3N_4, respectively.

Another material can be used as the waveguide layer, provided that its refractive index is larger than that of the CaF_2 substrate and its loss is low in the mid-IR. For example, Fig. 9(b) shows the transmission spectrum when a Si_3N_4 layer is used between the gold grating and the CaF_2 substrate. In this case, the geometric parameters are chosen to be: $\Lambda = 2.6$ μm, $t = 0.9$ μm, $w = 220$ nm, $d = 320$ nm, $h_1 = 50$ nm, and $h_2 = 250$ nm. Two ultra-narrow transmission dips can also be achieved. However, compared with those in Fig. 9(a), the Q-factors in Fig. 9(b) decrease to some extent. This is because the resonant electromagnetic fields in the Si_3N_4 layer are distributed closer to gold strips, and the loss becomes higher. Therefore, the refractive index of the waveguide layer has a distinct effect on the Q-factors.

Finally, these ultra-high resolving power filters are typically used in applications such as laser filtering and atomic/molecular line operating, so their operating wavelengths and lineshapes are crucial. We have investigated the use of two gold strips with different heights to introduce asymmetry in each unit cell, which can produce two resonances. Alternatively, the use of two unequal-width gold strips in each unit cell is also effective. From fabrication point of view, no matter which method of introducing asymmetry is used, the performance of such filters is inevitably very sensitive to fabrication errors due to their ultra-high Q-factors. Because it is difficult to overcome random errors in fabrication processes, remanufacturing could be time-consuming, costly, and even

ineffective. Perhaps post-processing is an essential and effective step to achieve desired operating wavelengths and lineshapes. In the case of using two unequal-width gold strips in each unit cell, the operating lineshapes are determined by the center-to-center distance between the two gold strips (not shown). We will not be able to adjust the operating lineshapes of such a filter through post-processing. However, in the case of the present configuration, both the operating wavelengths and lineshapes of a fabricated filter can be flexibly adjusted through post-processing (for example, milling the gold strips from the top using a focused ion beam).

4. Conclusion

In summary, we have designed a mid-IR dual-band filter, which consists of an Al_2O_3 layer between a subwavelength periodic gold grating and a CaF_2 substrate. Each unit cell of the grating is composed of two gold strips with different heights. The transmission spectrum of the filter shows only two ultra-narrow dips over a broad spectral region. One is at a wavelength of $\sim$3.8392 μm with a FWHM of $\sim$0.8 nm, and the other is at a wavelength of 3.8435 μm with a FWHM of $\sim$1.8 nm. Thus, the filter has an ultra-high resolving power. FDTD simulations reveal that the two dips result from the $(+1)$ and (-1) waveguide modes, respectively. It is found that an interaction between the $(+1)$ and (-1) modes exists. The interaction affects the FWHMs and lineshapes of the two bands, and can be controlled by adjusting the grating parameters. Therefore, we can design the FWHMs and lineshapes of the two bands flexibly. Moreover, from fabrication point of view, some typical cases have been investigated. The results indicate that the designed structure is also effective in the presence of fabrication errors and has a good expansibility. This work offers an approach to the design of high resolving-power dual-band filters for multi-spectral control of mid-IR signals.

References

[1] C.-S. Im and S.-S. Lee, "Highly efficient and angle-tolerant mid-infrared filter based on a cascaded etalon resonator," *Opt. Express*, vol. 25, no. 14, pp. 16083–16091, 2017.

[2] Z. Y. Wang, R. J. Zhang, and J. P. Guo, "Quadrupole mode plasmon resonance enabled subwavelength metal-dielectric grating optical reflection filters," *Opt. Express*, vol. 26, no. 1, pp. 496–504, 2018.

[3] D. L. Brundrett, E. N. Glytsis, and T. K. Gaylord, "Normal-incidence guided-mode resonant grating filters: Design and experimental demonstration," *Opt. Lett.*, vol. 23, no. 9, pp. 700–702, 1998.

[4] S. S. Wang and R. Magnusson, "Theory and applications of guided-mode resonance filters," *Appl. Opt.*, vol. 32, no. 14, pp. 2606–2613, 1993.

[5] Z. S. Liu, S. Tibuleac, D. Shin, P. P. Young, and R. Magnusson, "High-efficiency guided-mode resonance filter," *Opt. Lett.*, vol. 23, no. 19, pp. 1556–1558, 1998.

[6] G. Chen, K. J. Lee, and R. Magnusson, "Periodic photonic filters: Theory and experiment," *Opt. Eng.*, vol. 55, no. 3, 2016, Art. no. 037108.

[7] T. Xu, Y.-K. Wu, X. Luo, and L. J. Guo, "Plasmonic nanoresonators for high-resolution colour filtering and spectral imaging," *Nature Commun.*, vol. 1, pp. 1–5, 2010, Art. no. 59.

[8] E. Li, X. Chong, F. Ren, and A. X. Wang, "Broadband on-chip near-infrared spectroscopy based on a plasmonic grating filter array," *Opt. Lett.*, vol. 41, no. 9, pp. 1913–1916, 2016.

[9] H. S. Lee, Y. T. Yoon, S. S. Lee, S. H. Kim, and K. D. Lee, "Color filter based on a subwavelength patterned metal grating," *Opt. Express*, vol. 15, no. 23, pp. 15457–15463, 2007.

[10] G. Hawkins, R. Sherwood, and K. Djotni, "Mid-infrared filters for astronomical and remote sensing instrumentation," *Proc. SPIE*, vol. 7101, 2008, Art. no. 710114.

[11] Y. Zhong *et al.*, "Mid-wave infrared narrow bandwidth guided mode resonance bandstop filter," *Opt. Lett.*, vol. 42, no. 2, pp. 223–226, 2017.

[12] J.-N. Liu, M. V. Schulmerich, R. Bhargava, and B. T. Cunningham, "Sculpting narrowband Fano resonances inherent in the large-area mid-infrared photonic crystal microresonators for spectroscopic imaging," *Opt. Express*, vol. 22, no. 15, pp. 18142–18158, 2014.

[13] W. X. Liu, Z. Q. Lai, H. Guo, and Y. Liu, "Guided-mode resonance filters with shallow grating," *Opt. Lett.*, vol. 35, no. 6, pp. 865–867, 2010.

[14] J.-N. Liu, M. V. Schulmerich, R. Bhargava, and B. T. Cunningham, "Optimally designed narrowband guided-mode resonance reflectance filters for mid-infrared spectroscopy," *Opt. Express*, vol. 19, no. 24, pp. 24182–24197, 2011.

[15] A. Feng, Z. Yu, and X. Sun, "Ultranarrow-band metagrating absorbers for sensing and modulation," *Opt. Express*, vol. 26, no. 22, pp. 28197–28205, 2018.

[16] E. Sakat *et al.*, "Free-standing guided-mode resonance band-pass filters: From 1D to 2D structures," *Opt. Express*, vol. 20, no. 12, pp. 13082–13090, 2012.

[17] K. Chen, R. Adato, and H. Altug, "Dual-band perfect absorber for multispectral plasmon-enhanced infrared spectroscopy," *ACS Nano*, vol. 6, no. 9, pp. 7998–8006, 2012.
[18] R. Feng, W. Ding, L. Liu, L. Chen, J. Qiu, and G. Chen, "Dual-band infrared perfect absorber based on asymmetric T-shaped plasmonic array," *Opt. Express*, vol. 22, no. S2, pp. A335–A343, 2014.
[19] X. Liu, J. Gao, H. Yang, X. Wang, and C. Guo, "Multiple infrared bands absorber based on multilayer gratings," *Opt. Commun.*, vol. 410, pp. 438–442, 2018.
[20] E. D. Palik, *Handbook of Optical Constants of Solids*. San Diego, CA, USA: Academic Press, 1998.
[21] M. N. Polyanskiy, Refractive index database. [Online]. Available: https://refractiveindex.info Accessed on Sep. 24, 2019.
[22] Y. Wang, J. Song, L. Dong, and M. Lu, "Optical bound states in slotted high-contrast gratings," *J. Opt. Soc. Amer. B*, vol. 33, pp. 2472–2479, 2016.
[23] E. N. Bulgakov and D. N. Maksimov, "Avoided crossings and bound states in the continuum in low-contrast dielectric gratings," *Phys. Rev. A*, vol. 98, 2018, Art. no. 053840.
[24] E. Bulgakov, D. Maksimov, P. Semina, and S. Skorobogatov, "Propagating bound states in the continuum in dielectric gratings," *J. Opt. Soc. Amer. B*, vol. 35, pp. 1218–1222, 2018.
[25] K. Koshelev, S. Lepeshov, M. Liu, A. Bogdanov, and Y. Kivshar, "Asymmetric metasurfaces with high-Q resonances governed by bound states in the continuum," *Phys. Rev. Lett.*, vol. 121, 2018, Art. no. 193903.
[26] Z. Zhang, Q. Yang, M. Gong, and Z. Long, "Toroidal dipolar bound state in the continuum and antiferromagnetic in asymmetric metasurface," *J. Phys. D: Appl. Phys.*, vol. 53, 2020, Art. no. 075106.
[27] X. Cui, H. Tian, Y. Du, G. Shi, and Z. Zhou, "Normal incidence filters using symmetry-protected modes in dielectric subwavelength gratings," *Sci. Rep.*, vol. 6, 2016, Art. no. 36066.
[28] D. B. Mazulquim *et al.*, "Efficient band-pass color filters enabled by resonant modes and plasmons near the Rayleigh anomaly," *Opt. Express*, vol. 22, no. 25, pp. 30843–30851, 2014.
[29] Y.-L. Liao, Y. Zhao, X. Zhang, and Z. Chen, "An ultra-narrowband absorber with a compound dielectric grating and metal substrate," *Opt. Commun.*, vol. 385, pp. 172–176, 2017.
[30] R. Boidin, T. Halenkovič, V. Nazabal, L. Beneš, and P. Němec, "Pulsed laser deposited alumina thin films," *Ceram. Int.*, vol. 42, no. 1, pp. 1177–1182, 2016.
[31] K. Luke, Y. Okawachi, M. R. E. Lamont, A. L. Gaeta, and M. Lipson, "Broadband mid-infrared frequency comb generation in a Si_3N_4 microresonator," *Opt. Lett.*, vol. 40, no. 21, pp. 4823–4826, 2015.